https://doi.org/10.1016/j.electacta.2019.02.106

On-Chip Suspended Gold Nanowire Electrode with Rough Surface: Fabrication and Electrochemical Properties

Yao Gao [a, b], Sheng Sun [a], San-Qiang Shi [b], Francesco Ciucci [c] and Tong-Yi Zhang [a, *]

[a] Materials Genome Institute, Shanghai University, 333 Nanchen Road, Shanghai, China

[b] Department of Mechanical Engineering, The Hong Kong Polytechnic University, Hung Hom, Kowloon, Hong Kong, China

[c] Department of Mechanical and Aerospace Engineering, The Hong Kong University of Science and Technology, Clear Water Bay, Kowloon, Hong Kong, China

*Corresponding author. Materials Genome Institute, Shanghai University, 333 Nanchen Road, Shanghai, China

Email address: zhangty@shu.edu.cn (T. Zhang).

Declarations of interest conflict: none.

Abstract: Nanoporous materials have attracted great attention due to the large ratio of surface over volume. Similarly, nanomaterials with big surface roughness have also high surface/volume ratio. The present work investigates the electrochemical behavior of nanowire electrode with big surface

roughness. An on-chip individually addressable suspended gold nanowire (width: 340 nm, thickness: 90 nm, and length: 5.5 μm) electrode with an arithmetic mean surface roughness of 15.02 ± 2.95 nm was fabricated by using the electron beam lithography and reactive ion etching technique. The Cyclic Voltammogram (CV) of the suspended Au nanowire electrode in sulfuric acid electrolyte shows noticeably different characteristics in terms of the number and shape of current spikes from that of the control Au thin film electrode. The suspended nanowire shows an excellent room-temperature cyclic reliability, with only ±3% variation in the integrated capacitance after 600 cycles at the scanning rate of 0.1 Vs^{-1}. The facile on-chip fabrication, large effective surface area, and excellent cyclic stability make suspended gold nanowire electrode an ideal candidate for many emerging applications such as electrochemical catalysts, biosensors, and detectors.

Keywords: suspended nanowire, roughness, cyclic voltammetry, electrochemical impedance spectroscopy, double layer capacitance

1. Introduction

The use of nanoscale materials as building blocks in nanoelectromechanical systems enables integrated circuit miniaturization and has initiated the rapid development in analytical techniques.[1, 2] The advantages of nanoelectrode, such as the reduction in response time, the enhancement in mass transport efficiency, the improvement in signal-to-noise ratio, highlight its applicability to sensors and detectors.[3] Nanoelectrodes are generally defined as electrodes having at least one dimension in the sub-100 nm range.[4] Nanoelectrode geometries include disks,[5] recessed bands,[6] nanowires (NW),[7] etc.; among them, NW electrodes attract lots of

interests due to their rapid mass transport (by virtue of width) and relative large current (by virtue of length).

The preparation of nanowire electrodes can be done by the “bottom-up” method or the “top-down” approach. The "bottom-up" approach first requires the fabrication of nanowires by chemical/electrochemical synthesis methods. Nanowires prepared by the "bottom-up" approach usually have the desired shape, composition and crystal structure but require additional steps to be used as electrodes: for example, nanowire transfer and electrical conductance realization. Nanowire transfer is commonly accomplished by dropping a small amount of a nanowire suspension solution onto a surface containing preformed contact pads.[8] Statistically, some nanowires will fall onto desired positions. In the study of the electrochemical behavior of a single nanowire electrode, the nanowire transfer can be performed by a nanomanipulator, but it will be very time consuming and highly demanding for operational experience. An electric contact can be established to the bottom-up prepared NWs by depositing metal pads (e.g. Pt, Ag) by focused ion beam (FIB)[9] or by electron beam lithography (EBL) [10] at its one or two ends. To use a single nanowire as the electrode, representative fabrication methods also include micropipette pulling technology,[11] and partial insulation of a sharpened wire/fiber in photoresist,[12] Teflon[13], electrophoretic paint,[14] and glass.[15] An overall disadvantage of these methods is that it is difficult to use these methods in mass production, and many steps are overly dependent on the operator's experience (such as the polishing step in the micropipette pulling technology). Moreover, these methods make it almost impossible to prepare nanoelectrode arrays with clear positional alignment requirements.

In the top-down approach, samples are evaporated, deposited and patterned into desired shapes from thin films or even bulk materials, where the representative technologies include

nanoskiving,[16] lithographically patterned nanowire electrodeposition (LPNE),[17] nanoimprint lithography,[18] focused ion beam (FIB) [19] and electron beam (E-beam) lithography.[20] The nanoskiving technique uses an ultramicrotome to section thin films of metal embedded in a polymer matrix.[16] The LPNE method unites characteristics of photolithography with the adaptability of bottom-up electrochemical synthesis: photolithography determines the position of the nanowires, and the duration of electrodeposition determines the width of the nanowires.[17] The approach of nanoprint uses compression molding to generate a pattern with thickness contrast in a thin resist film coated on a substrate, then an anisotropic etch is conducted to transfer the pattern through the entire resist thickness.[18] The FIB technique is performed by selectively milling out the silicon nitride passivation layer by a focused gallium ion beam to expose the underlying metal film.[21] The EBL method draws a custom shape on the electronically sensitive film by changing the solubility of the area exposed to the electron beam, and by immersing it in a specific solvent, the exposed or unexposed areas can be selectively removed.[1]

The top-down approaches show promise for mass production of nanoelectrodes and nanoelectrode arrays compared to bottom-up methods. Nanoelectrodes can be easily fabricated into different shapes with precise control of geometry and alignment. Nanoelectrodes can also be fabricated with other functional electrical components to achieve a variety of functions and applications.[22] Furthermore, the top-down prepared nanoelectrodes do not require further mechanical polishing steps, which greatly improves repeatability and reduces the dependency of manual operations. These mentioned top-down fabrication techniques have been widely employed to prepare electrically addressable nanowire electrodes or electrode arrays supported on a substrate. However, the electrochemical behavior of on-chip suspended nanowires (supported at both NW ends) has not been reported yet. In this paper, we used a combined method of EBL and

photolithography to prepare a suspended gold nanowire electrode with a well-defined electrochemically accessible region. By simply changing the exposure mask patterns, this method can also be used to prepare suspended nanowire electrode arrays, that in which each NW is individually addressable.

The effective surface area of electrodes plays a crucial role in the surface based electrochemical analytical and capacitive applications.[23-30] Therefore, great attempts have been done to prepare macroporous Au ultramicroelectrodes,[31] nanoporous Au microelectrode,[32] and suspended nanoporous Au films.[33] Increasing NW surface roughness is one of the most convenient and effective ways to achieve a higher effective surface area without sacrificing the mechanical stiffness and adding more mass to the system. In this paper, the reactive ion etching (RIE) technique was adopted to increase the surface roughness of the prepared nanowire electrode.

The electrochemical behavior of the prepared Au NW electrode is characterized by cyclic voltammetry (CV) and electrochemical impedance spectroscopy (EIS) tests with electrolyte of the potassium ferricyanide solution and the sulfuric acid solution, respectively. The choice of gold as the working electrode is based on the following considerations: Au has low cytotoxicity, weak chemisorption, poor oxidizability, good catalytic properties towards oxidation of carbon oxide and glucose, and high affinity to molecules containing thiol/amine functional groups. The mass transport method, adsorption/desorption process of anions on the Au electrode surface, the charge/discharge process of the electrochemical double layer (EDL), and the redox reaction of gold can also be evaluated by the designed CV and EIS tests.[33]

In this article, we prepared on-chip individually addressable suspended gold nanowire electrodes (length: 5.5 μm, width: 340 nm and thickness: 90 nm) with rough surface by using a combined method of E-beam lithography and photolithography. The structure and surface morphology of the

prepared electrode were characterized by the scanning electron microscope (SEM) and the atomic force microscope (AFM). The electrochemical performance of the prepared Au NW electrode, including the faradaic behavior, the capacitive behavior and the cycling stability, were thoroughly investigated by CV and EIS tests at room temperature.

2. **Experimental**

2.1 Sample Fabrication

The process flow for preparing the suspended Au NW electrode is shown in Fig. 1. The substrate used was a four-inch silicon (100) wafer (Fig. 1(a)). Before processing, the wafer was cleaned sequentially in 90 vol% H_2SO_4 solution (120 ℃, 10 min), DI water (4 cycles of dump rinse), 2 vol% HF solution (25 ℃, 1 min) and DI water (4 cycles of dump rinse). Then a layer of SiO_2 (thickness: 1 μm) was grown on the silicon wafer in the diffusion furnace, succeeded by the deposition of a layer of Si_3N_4 (thickness: 100 nm) in the low pressure chemical vapor deposition furnace (ASM LB45 LPCVD Furnace) (Fig. 1(b)). The thickness ratio of SiO_2 to Si_3N_4 was selected to be 10:1 to achieve a balance of residual stress.

The wafer was then primed with HDMS (hexamethyldisilazane) for 10 min in a vacuum desiccator. The photoresist ZEP-520 (thickness: 180 nm) was spin-coated on the wafer and baked at 200 ℃ for 2 min. Then the photoresist PMMA (polymethylmethacrylate, thickness: 80 nm) was spin-coated to form a bilayer-photoresist together with the previously coated ZEP-520 (Fig. 1(c)). The step of exposure was conducted with an electron beam (EBL_JBX-6300FS, JEOL Ltd., Japan, dose: 50 μCcm^{-2}) (Fig. 1(d)) and the exposed regions of photoresists would be dissolved away in the developer Xylene (20 ℃, 40 s) (Fig. 1(e)). After that, the wafer was first rinsed in IPA (isopropyl alcohol): MIBK (methyl isobutyl ketone, volume ratio: 3:1, 30 s), and then rinsed in IPA (30 s) and dried with nitrogen gas. The Ti (adhesion layer, thickness: 10 nm) and Au (thickness:

90 nm) were sequentially deposited at a rate of 1 As^{-1} (AST Peva-600EI) (Fig. 1(f)). The residual photoresist was then completely stripped in N-methyl-2-pyroridone at 50 ℃ for 15 min. The Au/Ti carried on the photoresist was also stripped away, leaving only the area exposed to the electron beam to be covered by Au/Ti (Fig. 1(g)). This process is regarded as the lift-off approach. Each 4-inch silicon wafer was divided into 7 x 7 = 49 sub-areas, and every sub-area was treated as a separate chip (as shown in Fig. S1). The pattern design of a single chip is shown in Fig. S2(a). At each chip center, six NWs having the same geometrical dimensions (width: 340 nm, thickness: 90 nm, length: 10 μm, the distance between neighboring NWs: 3.5 μm) were prepared (Fig. S2(b)).

The contact pads and circuit traces were prepared using the photolithography lift-off technique. The wafer was primed with HDMS (hexamethyldisilazane, 10 min) in a vacuum desiccator. Photoresist HPR 504 (thickness: 1.3 μm) was spin-coated on the wafer and soft baked (110 ℃, 1min). The pattern was exposed with mask aligner (Karl Suss MA6) to ultraviolet light through quartz patterned mask (5 s). During development in FHD-5 solution (1 min), the photoresist was removed from areas exposed to the ultraviolet light. The wafer was rinsed in DI water (4 cycles of dump rinse) and dried, and then hard baked in an oven (120 ℃, 30 min). Ti (adhesion layer, thickness: 20 nm) and Au (thickness: 500 nm) were sequentially deposited (AST Peva-600EI, rate: 1 As^{-1}). The strip of photoresist was processed in acetone (20 min). The wafer was rinsed in IPA (2 min) and DI water (1 min) and dried with nitrogen gas. With the help of alignment marks, contact pads for electrical connection were overlaid at both terminals of each NW electrode to realize the electrical conductivity as shown in Fig. S2(b) and Fig. 1(h).

A layer of SiO_2 (thickness: 500 nm) was deposited using the plasma-enhanced chemical vapor deposition (PECVD) method (Fig. 1(i)). Then the photoresist HPR 504 (thickness: 1 um) was spin-coated on the wafer (Fig. 1(j)). Sequentially, the wafer was soft baked (110 ℃, 1min), exposed to

UV light (5 s), developed in FHD-5 (1 min), rinsed in DI water (4 cycles of dump rinse), hard baked (120 ℃, 30 min) and then formed the structure shown in Fig. 1(k). The width of the open window as shown in Fig. 1(k) and Fig. S2(a) determines the suspended length of the NW after the reactive ion etching (RIE) step and was set as 5.5 μm. A series of RIE (Oxide RIE Etcher, Oxford) processes were employed to create the suspension structure of the Au NW, including anisotropic and isotropic etching steps (Fig. 1(l)). Firstly, an etching recipe of a mixture of gases CHF_3 and O_2 was used to anisotropically etch away the SiO_2 layer grown by the PECVD. Then a descum process was adopted to clean the surface. A mixture of gases He and SF_6 was used to etch away the Si_3N_4 layer (grown by LPCVD) and a mixture of gases SF_6 and O_2 was used to isotropically etch away the SiO_2 layer (grown in the diffusion furnace) to make the NW suspended. Then the Ti layer was etched by a mixture of Cl_2 and Ar. When this step was finished, the contact pads were exposed and the Au NW was suspended.

The wafer was diced along the boundaries between the chips and each chip was assembled onto a specially designed printed circuit board (PCB) (Fig. 1(m)) and wire bonded to 25 μm aluminum wire (Fig. 1(n)). Then the contact wires with insulating sleeves were soldered onto the PCB (Fig. 1(o)) and the assembled chip was insulated with the encapsulant (CHIPCOAT G8345-6 and CHIPCOAT G8345-D) leaving only the electrode area electrochemically accessible (Fig. 1(p)). Fig. 2(a) is an optical photograph of the sample after final packaging. A top view of the central portion of the packaged test device is shown in Fig. 2(b). Fig. 2(c) shows a schematic cross-sectional view of the test device (ignoring the bonded and soldered contact wires).

To serve as the reference group, a supported Au thin film (TF) sample was also prepared in a manner similar to the NW sample by replacing the electron beam lithography step with a conventional photolithography process and also some adjustments in the RIE step.

2.4 Characterization

The surface morphology of prepared Au NW electrode was characterized by the SEM (JSM-7100F (JEOL)) with lower electron detector and backscattered electron detector. The suspended structure and the surface morphology of the prepared nanowire electrode was also characterized by the AFM (Veeco MultiMode Scanning Probe Microscope). The employed AFM tip (Bruker MPP-21120-10) is made of phosphorous doped silicon and mounted on a rectangular cantilever with an original tip radius of ~8 nm. The AFM topography image of the suspended gold nanowire was obtained in the contact mode with a scan rate of 0.1 Hz and a set point of 1.0 V before the chip was assembled to the PCB. The functionality of the fully packaged device was evaluated by the standard two-point *I-E* test with a voltage bias of ±20 mV.

2.5 Chemicals and Experiments

H_2SO_4 (98%), KCl (99%) and $K_3[Fe(CN)_6]$ (99%) were purchased from Sigma-Aldrich. Deionized water (18.2MΩ resistivity, Milli-Q, Millipore) was used for all experiments. All reagents were of analytical grade and were used without further purification. Electrochemical measurements including CV and EIS tests, were performed using a personal computer controlled CHI760D electrochemical workstation (CH Instruments, Inc., USA). The traditional three-electrode system was used in the tests, with Au NW as the working electrode, Ag/AgCl (with saturated KCl) as the reference electrode and a platinum wire as the counter electrode. The prepared chips were thoroughly cleaned by continuously immersing in ethanol and deionized water each for 10 minutes, dried first with a nitrogen gun and then left in a vacuum oven at 60 ℃ for 1 hour. The electrolyte was degassed by bubbling N_2 (20 min) prior to measurement and the nitrogen flow was stopped throughout the measurement to avoid possible damages to the suspended

nanowire. Prior to the electrochemical test, the Au NW electrodes were cyclically scanned in H_2SO_4 solution (0.1 M) from 0 V to +1.5 V until a reproducible voltammogram was observed. During the EIS tests, the external potential was chosen from 0 V to 0.8 V with an interval of 0.1 V. Frequency was swept from 60 kHz to 100 Hz, and a 10 mV rms perturbation signal was applied.

3. Results and Discussion

As shown in Fig. 3(a), the SEM image taken at tilted angles verifies the suspension state of the NW. The SEM images in Fig. 3(b) and 3(c) show that the prepared Au NW has a rough surface. This surface morphology is very similar to the morphology of nanoporous materials.[32, 34, 35] Based on the difference in contrast, the average size of the convex and the concave on the NW surface is statistically measured to be 60.52 ± 9.01 nm and 42.67 ± 3.05 nm, respectively. Fig. 3(d) is an AFM scanning image of one Au NW in which four scanning lines are selected, and the corresponding height profiles are plotted in Fig. 3(e) and Fig. 3(f). The height differences between the peak and baseline of curves AA' and BB' are ~350 nm and the height differences between the plateau region of curves CC' and DD' exhibit similar values of ~341 nm. Since the thickness of the nanowire is only ~90 nm, the free-standing structure of the nanowire is verified. Based on the obtained AFM topography image, the arithmetic mean surface roughness and the arithmetic mean line roughness of the gold nanowires were calculated to be 15.02 ± 2.95 nm and 18.99 ± 2.10 nm, respectively, by AFM image analysis software (Nanoscope 8.0).

The functionality of the fully packaged device was evaluated by the standard two-point I-E test. As shown in Fig. S3, all test samples display an Ohmic linear response with a voltage bias of ±20 mV, confirming good electrical contacts with the electrodes through the prepared circuit traces and bonding wires. The insulating properties of the thermally grown SiO_2 and Si_3N_4 layers are verified by the ultrahigh resistances measured from the control devices in absence of Au NWs. A

total of 18 nanowires on three chips (6 NWs on each chip) were evaluated by the I-E tests, and 10 of them were successfully suspended, with a total manufacturing success rate of 55.56%. The success rate of each chip is 50%, 50% and 67.67%.

3.1 Comparison of electrochemical behavior of suspended Au NW and supported Au TF

The setup for the electrochemical test is shown in Fig. 4(a). The electrochemical behavior of prepared Au NW electrode is first evaluated in 20 mM $K_3[Fe(CN)_6]$ + 0.1 M KCl solution. The $[Fe(CN)_6]^{4+/3+}$ reaction in aqueous solution involves the transfer of a single electron and serves as a standard reaction in fundamental electrochemistry. Fig. 4(b) and 4(c) show CV curves obtained from the NW electrode at scan rates ranging from 500 mVs^{-1} to 20 mVs^{-1} and from 10 mVs^{-1} to 2 mVs^{-1}, respectively. In order to make a comparison, similar tests are conducted on the supported Au TF electrode and the obtained voltammograms are shown in Fig. 4(d) and Fig. 4(e). The nanowire electrode is a two-dimensional system behaving much like the cylindrical microelectrode, whose diffusion current is composed of the planer linear diffusion term with a correction term (also referred to as the steady-state term).[36] The addition of the correction term is due to the fact that the growth of the depletion region fails to affect the concentration gradients at the nanowire's surface because the diffusion field is able to draw material from a continually larger area at its edge.[36] When the mass transport to the electrode is dominated by the planar linear diffusion, the voltammogram shows clear peak-shaped, as the voltammograms obtained from the Au TF sample shown in Fig. 4(d) and Fig. 4(e). And when the mass transport is dominated by the correction term (radial diffusion), S-shaped voltammogram is obtained. As shown in Fig. 4(b), the voltammograms obtained from the Au NW electrode are the overlay of the S-shaped voltammogram and the peak-shaped voltammogram. However, for the NW electrode, the peaks are not clear even with the scan rate of 500 mVs^{-1}, suggesting that the radial diffusion instead of

the linear diffusion is dominant within the measured scan rates for the suspended NW electrode. When the scan rate decreases, the contribution of radial diffusion continues to increase. When the scan rate is small enough, such as 2 mVs^{-1} as shown in Fig. 4(c), quasi steady state current is obtained.

For the Au NW and Au TF samples, the relationships between the peak-to-peak separation ΔE_p (definition is illustrated in Fig. S4) and the scan rate v are plotted in Fig. 4(f). It is found that the value of ΔE_p increases as the scan rate increases. As shown in Fig. 4(f), at the same scan rate, ΔE_p of the NW electrode is smaller than that of the TF electrode, indicating the $[Fe(CN)_6]^{3+/4+}$redox reaction is more reversible on the NW electrode than on the TF electrode. Furthermore, the ΔE_p of the NW is less dependent on the scan rate than the TF electrode. The increase in ΔE_p as v increases indicates that the $[Fe(CN)_6]^{3+/4+}$redox reaction becomes quasireversible when the scan rate is fast. In other words, as the scan rate increases, the rate of heterogeneous electron transfer starts to compete with the rate of potential change. When the mass transfer of the system is controlled by the planar linear diffusion, the standard heterogeneous rate constant k_0 of the reaction can be evaluated from the relationship between ΔE_p and v following the Nicholson method [37] (see supporting information for more details).

Voltammograms are widely used as fingerprints for electrode-electrolyte systems because they are ultrasensitive to electrode/electrolyte interface structures. Fig. 5(a) and Fig. 5(b) show the voltammograms obtained from the Au NW electrode at a scan rate of 0.1 V s^{-1} at voltage range of [0 V - 1.55 V] and [0 V - 0.8 V], respectively. Unlike the voltammogram obtained from the Au TF sample (see Fig. S6), when we examine the CV curves obtained from the suspended Au NW electrode, the current peaks (peaks labelled as P_1 and P_2 in Fig. S6) corresponding to the formation/lifting of the Au(111) reconstruction are disappeared. There are two possible reasons

for these two peaks to disappear in the voltammogram of the suspended Au NW electrode. Firstly, the x-ray diffraction[38] and scanning tunneling microscopy[39] tests show that the average domain width for the reconstructed herringbone structure is around 15nm, which means that the rough NW electrode surface may not be able to provide sufficient long-range ordered regions for the surface reconstruction. The other reason is that, without the long-range elastic interactions mediated by the substrate, the suspended Au NW electrode fails to form "stress domains" which is necessary for the ($\sqrt{\mathbf{3}} \times 22$) reconstruction.[40]

A series of peaks (labeled P_{O1} and P_{O2}) appear above ~1.0 V in the positive sweep segment, corresponding to intermediate steps in forming the gold oxide layer. By comparing Fig. 5(a) and Fig. S6(a), we find obvious differences in performances of Au NW and Au TF electrodes within this potential region. In the voltammogram obtained from the Au NW electrode in 0.01 M H_2SO_4 solution, there are two gentle oxidation peaks centered at 1.06 V and 1.28 V, which are the characteristic peaks of the (100) and the (111) crystal planes, respectively. The voltammogram obtained from the Au NW electrode in 0.1 M H_2SO_4 solution at 0.1 Vs^{-1} has only one distinct oxidation peak centered at 1.35 V, which is characteristic of the (111) crystal plane. Different from the single reduction peak of Au TF sample as shown in Fig. S6(a), there are two reduction peaks (labeled as P_{R1} and P_{R2}) in the negative sweep segment of voltammograms of Au NW electrode in 0.1 M H_2SO_4 solution (as shown in Fig. 5(a)). In the CV curve obtained from the 0.01 M H_2SO_4 solution, the current spike P_{R2} turns into a plateau. Compared to the reported CV curves of the Au(111), Au(100), and Au(110) surfaces,[35] only those curves obtained from the Au(110) surface show a second current spike or plateau in the negative sweep segment and was attributed to the stepwise reduction of the gold oxide.[39] However, in the literature, the magnitudes of the second

reduction spike are all much smaller compared to the first reduction spike, which is different from our situation.

The enhancement of peak P_{R2} in voltammograms obtained from the Au NW electrode may be induced by the effect of "selective augment of sluggish faradaic reactions": due to the nanoconfinement of a rough electrode surface, the augment of the slower electron transfer reaction will be more pronounced than the reaction with a faster electron transfer rate.[41] The slower charge transfer reaction makes unreacted molecules more likely to survive in deeper parts of the surface. The high concentration of the reactive molecules in these recessed portions of the electrode surface enables the sluggish electron transfer reaction to occur on almost the entire electrode surface. On the other hand, the surface area available for the fast electrochemical reaction (which is usually diffusion controlled) is mainly limited to the outermost region of the electrode. As a result, the surface area participating in the slow reaction is even larger than the surface area involved in the fast electron transfer reaction. The unique properties of this rough surfaced gold nanowire electrode make it an ideal choice for sensors and detectors because it allows those invisible reactions to be detected.

The excess charges on the electrode surface induce an unequal distribution of anions and cations in the electrolyte near the electrode surface and result in the occurrence of the EDL. By comparing Fig. 5(b) and the Fig. S6(b), it can be found that the charge/discharge current within the EDL region of the Au NW electrode shows a stronger potential dependence than the Au TF electrode. The deviation of the CV curve from the rectangle to the lens-shape has been widely observed in porous material based supercapacitors.[42] Considering that the prepared Au NW electrode has a morphology similar to that of a nanoporous material (high surface roughness and uniformly distributed protrusions and depressions), the possible reason for this deformation of the CV shape

can be that the charge/discharge of the EDL consists of multiple steps with different time constants. At higher scan rate, the failure to catch up with the potential perturbation will result in the hysteresis between the charging and discharging sweep segments.[43]

Fig. 5(c) and (d) show the voltammograms of free-standing Au NW electrode at different scan rates in 0.1 M and 0.01 M sulfuric acid solutions, respectively. Fig. S7 shows the voltammograms of the Au TF sample in 0.1 M sulfuric acid solution obtained at different scan rates. As shown in Fig. 5(e), for peak P_{R1}, the slopes of $\log i_p$ *vs*. $\log v$ of Au NW electrode are calculated to be 0.67 and 0.58 in 0.1 M and 0.01 M H_2SO_4 solutions, respectively. And for the Au TF sample, the slope of $\log i_p$ *vs*. $\log v$ is calculated to be 0.67. These data indicate that the reduction of gold oxide in both 0.1 M and 0.01 M H_2SO_4 solutions are controlled by both diffusion and adsorption. Fig. 5(f) shows a plot of peak potentials of P_{R1} vs. $\ln v$, which gives straight lines with slopes of -0.029 (Au TF, 0.1 M), -0.021 (Au NW, 0.1 M) and -0.037 (Au NW, 0.01 M). These slopes are varied between the range of 0 and $2RT/F$, suggesting that the processes represented by these peaks are all quasi-reversible.

3.2 Capacitive behaviors of the Au NW electrode

Compared to the CV test, EIS is a powerful tool in investigating a system in which the conductivity is influenced by various microscopic processes that occur at different timescales. In addition, EIS allows one to evaluate the magnitude of a single impedance element at a higher resolution and at different external potentials.[44] Therefore, we conducted EIS tests to investigate the capacitive behavior of the prepared suspended Au NW electrode. The "equivalent circuit" method is adopted for the data analysis of the EIS test results. The underlying microscopic processes are represented by ideal circuit elements, respectively. By fitting the experimental results to this equivalent circuit, the values of these microscopic processes can be generated.[44] Different

weighting methods can be used during data fitting. Zoltowski[45] recommends that the choice of weighting type should be verified experimentally in each case. In our work, unity weighting is chosen as giving the smallest fitting errors. A variety of equivalent circuit models have been developed for different electrochemical systems. In the data analysis step, it is preferable to start with the simplest circuit and then add additional elements if necessary.[46]

Impedance data was obtained in H_2SO_4 solution at room temperature. As for our case, the Kovacs model (as illustrated in Fig. 6(a)) is first used for data fitting, which is one of the most common circuits for describing the electrochemical behavior of nanoelectrodes. It modifies the Randles' model by including a component of the Warburg impedance Z_W to represent the diffusion process. The elements C_{DL} and R_{ct} represent the double layer capacitance and the charge-transfer resistance of the adsorption process, respectively. The Warburg impedance is caused by the diffusion of ions from the bulk electrolyte to the interface.[47] The measured impedance results and the fitted curves based on the Kovacs model are presented in Fig. 6(b). The obtained C_{DL}^{eis} values are plotted against the potential in Fig. 6(c), and the average value in 0.1 M H_2SO_4 solution is 0.38 ± 0.048 nF. The superscript "eis" in symbol C_{DL}^{eis} indicates that this double layer capacitance value was obtained from the EIS experiment. The generated values of other circuit elements are listed in Table S1.

Considering the large surface roughness of our sample, its electrochemical behavior may be significantly different from that of the planar electrodes. The main difference is that the capacitive charge/discharge process of the rough electrode involves different time constants. These multi-time scale processes are typically described by a vertical ladder network of resistor-capacitor(RC)-series components.[48] Based on this consideration, the second circuit is constructed by adding an additional RC-series component to the Kovacs model as shown in Fig. 6(d). The new circuit is

referred to as the modified Kovacs model. The elements C_{DL1}, C_{DL2}, R_{DL} and R_{ct} represent the fast double layer capacitance, the slow double layer capacitance, the double layer charging resistance and the charge-transfer resistance of the adsorption process, respectively. The experimental data and fitting curves based on the modified Kovacs model are shown in Fig. 6(e). Table S2 and Table S3 list the generated values of each circuit elements. To justify the introduction of the additional RC-series component, we compared the chi-squared values obtained by the two circuits when fitting the data. It is found that for the data measured in 0.1 M and 0.01 M H_2SO_4 solutions, the chi-squared values of the modified Kovacs model are only 16.83% and 42.29% of the chi-squared values of the Kovacs model, respectively. These much smaller chi-squared values indicate that the modified Kovacs model is more suitable for our system than the Kovacs model and demonstrate the rationality of adding additional RC component in the equivalent circuit. The averaged values for C_{DL1} and C_{DL2} are plotted in Fig. 6(f). In order to better compare the capacitive behavior in different concentrations of H_2SO_4 solutions, we used an approximation to assume that $C_{DL}^{eis} = C_{DL1} + C_{DL2}$,[43] and the obtained value of C_{DL}^{eis} is also plotted in Fig. 6(f). When the concentration of sulphuric acid solution decreases from 0.1 M to 0.01 M, C_{DL1} decreases from 0.14 ± 0.0011 nF to 0.085 ± 0.0014 nF and C_{DL2} increases from 0.42 ± 0.12 nF to 0.47 ± 0.097 nF. However, at both concentrations, the value of C_{DL} remains almost unchanged: 0.56 ± 0.12 nF in 0.1 M H_2SO_4 solution and 0.55 ± 0.10 nF in 0.01 M H_2SO_4 solution. For both concentrations, C_{DL2} is much larger than C_{DL1}, which means the major part of the EDL capacitance occurs on a large timescale.

3.3 Cycling Performance

The cycling stability is one of the most important properties for the practical application of our prepared devices. The cycling performance was evaluated through CV tests conducted at room temperature. Fig. 7(a) and Fig. 7(b) present the voltammograms obtained at 0.1 Vs^{-1} in 0.1 M and

0.01 M H_2SO_4 solutions, respectively. For both concentrations, the shape of the CV curve slightly changes over the previous 150 sweep cycles and remains stable for the next 450 sweep cycles. The integrated capacitance for each sweep cycle is calculated following the equation of $C_{DL}^{i} = \frac{\int idE}{2v\Delta E}$ and the results are plotted against the number of sweep cycles in Fig. 7(c). In order to quantify the variation in the integrated capacitance, the obtained C_{DL}^{i} values shown in Fig. 7(c) are linearly fitted (the fitting curves are also shown in Fig. 7(c) as short dot lines). The change in capacitance is then calculated based on the first and the last points of the fitting curve. In both 0.1 M and 0.01 M H_2SO_4 solutions, the variation in the integrated capacitance was found to be only within ±3% at a scan rate of 0.1 Vs^{-1}, indicating that the prepared gold nanowire electrode has a great cycling stability. Similar cycling tests were also taken at 1.5 Vs^{-1} and the results are presented in Fig. S8.

4. Conclusion

In this paper, we present a feasible and highly reliable method for preparing on-chip suspended gold nanowire electrodes with rough surface. The CV and EIS tests were adopted to characterize the sample's electrochemical performances. Compared with the TF electrode, the NW electrode exhibits distinct electrochemical behaviors in both the potassium ferricyanide solution and the sulfuric acid solution: (1) within the scan rate range of 500 mVs^{-1} to 2 mVs^{-1}, the dominant mass transfer method is radial diffusion rather than planar linear diffusion; (2) the smaller peak-to-peak separation of the $[Fe(CN)_6]^{3+/4+}$redox reaction; (3) the disappearance of the current spike in the EDL region, which is attributed to the surface reconstruction of the Au (111) crystal plane; (4) the different shapes of the current peaks corresponding to the formation and reduction of the gold oxide; (5) the significant potential dependence of the EDL charge/discharge current and so on. The causes of these differences can be attributed to the effects of the suspended structure, the rough surface and the nanoscale geometry of the Au NW electrode. For example, the nanoscale geometry

leads to the enhanced mass transfer efficiency due to the radial diffusion and the rough surface results in the nanoconfinement effect. Two equivalent circuit were used for EIS data analysis: the Kovacs model and the modified Kovacs model. The modified Kovacs model adds a RC-series component to the Kovacs model to represent multiple time scales of the EDL charge/discharge process and shows a better fit to the experimental data. The cycling stability of the pseudocapacitive behavior is evaluated at room temperature. It was found that after 600 sweep cycles at 0.1 V s^{-1} in 0.1 M and 0.01 M H_2SO_4 solutions, the variation of integrated capacitance is less than ±3%.

The feasible on-chip fabrication method and the enhanced surface to volume ratio provide a means to apply a single nanowire electrode to an NEMS system. The high effective surface area and enhanced mass transfer efficiency due to the radial diffusion of the prepared suspended nanowire electrode results in an increase in the signal to noise ratio and an enhancement in the detection limit. The effect of selectively enhancing the slower Faraday reaction makes the original invisible reaction detectable and the disappearance of current spikes due to electrode surface reconstruction and structural changes in the anion adlayer makes our analysis of the target reaction more straightforward and simpler. These unique properties of suspended gold nanowire electrodes facilitate their use in the field of electrochemical analysis, including various detectors, sensors and multi-pixel imaging devices.

Supporting Information Available: See supplemental material for the details of the arrangement of chips in each 4-inch wafer, the pattern design of each chip, the results of I-E tests of the Au NWs, the illustration of the definition of the peak-to-peak separation, the generation of k_0 following the Nicholson's method, electrochemical test results of the Au TF sample in sulfuric

acid solution, voltammograms obtained from an Au FT electrode at different scan rates in sulfuric acid solution, the fitted values for the equivalent circuit elements, and the cycling test results obtained at 1.5 Vs^{-1} of the Au NW electrode. This material is available free of charge *via* the Internet at

Funding: This work was supported by the research grant [grant number 14DZ2261200] from the Science and Technology Commission of Shanghai Municipality.

Acknowledgements: The authors appreciated the technical assistance from the Materials Characterization and Preparation Facilities, the Center for Advanced Microsystems Packaging and the Nanoelectronic Fabrication Facility at Hong Kong University of Science and Technology and the facility support from the research group of Professor Y. Lu at the City University of Hong Kong.

REFERENCES

[1] Y. Gao, Y.-J. Sun, T.-Y. Zhang, Highly reliable and efficient atomic force microscopy based bending test for assessing Young's modulus of one-dimensional nanomaterials, Applied Physics Letters, 108 (2016) 123104.

[2] Y. Gao, S.-Q. Shi, T.-Y. Zhang, Adhesion contact deformation in nanobridge tests, Nanoscale, 9 (2017) 6033-6040.

[3] R.W. Murray, Nanoelectrochemistry: Metal nanoparticles, nanoelectrodes, and nanopores, Chem. Rev., 108 (2008) 2688-2720.

[4] J.T. Cox, B. Zhang, Nanoelectrodes: Recent Advances and New Directions, in: R.G. Cooks, E.S. Yeung (Eds.) Annual Review of Analytical Chemistry, Vol 5 (2012), pp. 253-272.

[5] Y. Zhang, S. Xu, Y. Qian, X. Yang, Y. Li, Preparation, electrochemical responses and sensing application of Au disk nanoelectrodes down to 5 nm, Rsc Advances, 5 (2015) 77248-77254.

[6] S.P. Mucelli, M. Zamuner, M. Tormen, G. Stanta, P. Ugo, Nanoelectrode ensembles as recognition platform for electrochemical immunosensors, Biosensors & Bioelectronics, 23 (2008) 1900-1903.

[7] H.-G. Im, S.-H. Jung, J. Jin, D. Lee, J. Lee, D. Lee, J.-Y. Lee, I.-D. Kim, B.-S. Bae, Flexible Transparent Conducting Hybrid Film Using a Surface-Embedded Copper Nanowire Network: A Highly Oxidation-Resistant Copper Nanowire Electrode for Flexible Optoelectronics, ACS Nano, 8 (2014) 10973-10979.

[8] T. Kim, A. Canlier, G.H. Kim, J. Choi, M. Park, S.M. Han, Electrostatic Spray Deposition of Highly Transparent Silver Nanowire Electrode on Flexible Substrate, ACS Applied Materials & Interfaces, 5 (2013) 788-794.

[9] B. Varghese, Y. Zhang, L. Dai, V.B.C. Tan, C.T. Lim, C.-H. Sow, Structure-Mechanical Property of Individual Cobalt Oxide Nanowires, Nano letters, 8 (2008) 3226-3232.

[10] E.K. McCarthy, A.T. Bellew, J.E. Sader, J.J. Boland, Poisson's ratio of individual metal nanowires, Nature Communications, 5 (2014).

[11] B.B. Katemann, W. Schuhmann, Fabrication and characterization of needle-type Pt-disk nanoelectrodes, Electroanalysis, 14 (2002) 22-28.

[12] P. Sun, Z.Q. Zhang, J.D. Guo, Y.H. Shao, Fabrication of nanometer-sized electrodes and tips for scanning electrochemical microscopy, Anal. Chem., 73 (2001) 5346-5351.

[13] B. Liu, J.P. Rolland, J.M. DeSimone, A.J. Bard, Fabrication of ultramicroelectrodes using a "Teflon-like" coating material, Anal. Chem., 77 (2005) 3013-3017.

[14] J.J. Watkins, J.Y. Chen, H.S. White, H.D. Abruna, E. Maisonhaute, C. Amatore, Zeptomole voltammetric detection and electron-transfer rate measurements using platinum electrodes of nanometer dimensions, Anal. Chem., 75 (2003) 3962-3971.

[15] B. Zhang, J. Galusha, P.G. Shiozawa, G.L. Wang, A.J. Bergren, R.M. Jones, R.J. White, E.N. Ervin, C.C. Cauley, H.S. White, Bench-top method for fabricating glass-sealed nanodisk electrodes, glass nanopore electrodes, and glass nanopore membranes of controlled size, Anal. Chem., 79 (2007) 4778-4787.

[16] M.D. Dickey, D.J. Lipomi, P.J. Bracher, G.M. Whitesides, Electrically Addressable Parallel Nanowires with 30 nm Spacing from Micromolding and Nanoskiving, Nano letters, 8 (2008) 4568-4573.

[17] E.J. Menke, M.A. Thompson, C. Xiang, L.C. Yang, R.M. Penner, Lithographically patterned nanowire electrodeposition, Nature materials, 5 (2006) 914-919.

[18] S.Y. Chou, P.R. Krauss, P.J. Renstrom, Imprint Lithography with 25-Nanometer Resolution, Science, 272 (1996) 85-87.

[19] R. Chen, K.K. Hu, Y. Yu, M.V. Mirkin, S. Amemiya, Focused-Ion-Beam-Milled Carbon Nanoelectrodes for Scanning Electrochemical Microscopy, Journal of the Electrochemical Society, 163 (2016) H3032-H3037.

[20] M.E. Sandison, J.M. Cooper, Nanofabrication of electrode arrays by electron-beam and nanoimprint lithographies, Lab on a Chip, 6 (2006) 1020-1025.

[21] Y.H. Lanyon, G. De Marzi, Y.E. Watson, A.J. Quinn, J.P. Gleeson, G. Redmond, D.W.M. Arrigan, Fabrication of nanopore array electrodes by focused ion beam milling, Anal. Chem., 79 (2007) 3048-3055.

[22] K. Ino, Microchemistry- and MEMS-based Integrated Electrochemical Devices for Bioassay Applications, Electrochemistry, 83 (2015) 688-694.

[23] B. Kirubasankar, P. Palanisamy, S. Arunachalam, V. Murugadoss, S. Angaiah, 2D MoSe2-Ni (OH) 2 nanohybrid as an efficient electrode material with high rate capability for asymmetric supercapacitor applications, Chemical Engineering Journal, 355 (2019) 881-890.

[24] A. Subasri, K. Balakrishnan, E.R. Nagarajan, V. Devadoss, A. Subramania, Development of 2D La(OH)3 /graphene nanohybrid by a facile solvothermal reduction process for high-performance supercapacitors, Electrochimica Acta, 281 (2018) 329-337.

[25] S. Vijayan, B. Kirubasankar, P. Pazhamalai, A.K. Solarajan, S. Angaiah, Electrospun Nd3+-Doped LiMn2O4 Nanofibers as High-Performance Cathode Material for Li-Ion Capacitors, ChemElectroChem, 4 (2017) 2059-2067.

[26] S. Arunachalam, B. Kirubasankar, V. Murugadoss, D. Vellasamy, S. Angaiah, Facile synthesis of electrostatically anchored Nd (OH) 3 nanorods onto graphene nanosheets as a high capacitance electrode material for supercapacitors, New Journal of Chemistry, 42 (2018) 2923-2932.

[27] B. Kirubasankar, V. Murugadoss, S. Angaiah, Hydrothermal assisted in situ growth of CoSe onto graphene nanosheets as a nanohybrid positive electrode for asymmetric supercapacitors, RSC Advances, 7 (2017) 5853-5862.

[28] B. Kirubasankar, V. Murugadoss, J. Lin, T. Ding, M. Dong, H. Liu, J. Zhang, T. Li, N. Wang, Z. Guo, S. Angaiah, In situ grown nickel selenide on graphene nanohybrid electrodes for high energy density asymmetric supercapacitors, Nanoscale, 10 (2018) 20414-20425.

[29] M. Kumar, A. Subramania, K. Balakrishnan, Preparation of electrospun Co3O4 nanofibers as electrode material for high performance asymmetric supercapacitors, Electrochimica Acta, 149 (2014) 152-158.

[30] K. Singh, B. Kirubasankar, S. Angaiah, Synthesis and electrochemical performance of P2-Na0.67AlxCo1-xO2 ($0.0 \leq \times \leq 0.5$) nanopowders for sodium-ion capacitors, Ionics, 23 (2017) 731-739.

[31] R. Szamocki, A. Velichko, C. Holzapfel, F. Mücklich, S. Ravaine, P. Garrigue, N. Sojic, R. Hempelmann, A. Kuhn, Macroporous ultramicroelectrodes for improved electroanalytical measurements, Anal. Chem., 79 (2007) 533-539.

[32] J. Jiang, X. Wang, L. Zhang, Nanoporous gold microelectrode prepared from potential modulated electrochemical alloying–dealloying in ionic liquid, Electrochimica Acta, 111 (2013) 114-119.

[33] H. Dong, X. Cao, Nanoporous gold thin film: Fabrication, structure evolution, and electrocatalytic activity, The Journal of Physical Chemistry C, 113 (2008) 603-609.

[34] T. Juarez, J. Biener, J. Weissmüller, A.M. Hodge, Nanoporous metals with structural hierarchy: A review, Advanced Engineering Materials, 19 (2017) 1700389.

[35] E. Rouya, S. Cattarin, M.L. Reed, R.G. Kelly, G. Zangari, Electrochemical Characterization of the Surface Area of Nanoporous Gold Films, Journal of the Electrochemical Society, 159 (2012) K97-K102.

[36] A.J. Bard, L.R. Faulkner, J. Leddy, C.G. Zoski, Electrochemical methods: fundamentals and applications, wiley New York1980.

[37] R.S. Nicholson, Theory and application of cyclic voltammetry for measurement of electrode reaction kinetics, Anal. Chem., 37 (1965) 1351-1355.

[38] J.V. Barth, H. Brune, G. Ertl, R.J. Behm, Scanning tunneling microscopy observations on the reconstructed Au(111) surface: Atomic structure, long-range superstructure, rotational domains, and surface defects, Physical Review B, 42 (1990) 9307-9318.

[39] K. Yoshida, A. Kuzume, P. Broekmann, I.V. Pobelov, T. Wandlowski, Reconstruction and electrochemical oxidation of Au (110) surface in 0.1 M H2SO4, Electrochimica acta, 139 (2014) 281-288.

[40] S. Narasimhan, D. Vanderbilt, Elastic stress domains and the herringbone reconstruction on Au (111), Physical review letters, 69 (1992) 1564.

[41] S. Park, H.C. Kim, T.D. Chung, Electrochemical analysis based on nanoporous structures, Analyst, 137 (2012) 3891-3903.

[42] C. Zequine, C.K. Ranaweera, Z. Wang, S. Singh, P. Tripathi, O.N. Srivastava, B.K. Gupta, K. Ramasamy, P.K. Kahol, P.R. Dvornic, R.K. Gupta, High Per formance and Flexible Supercapacitors based on Carbonized Bamboo Fibers for Wide Temperature Applications, Scientific Reports, 6 (2016) 31704.

[43] S. Fletcher, V.J. Black, I. Kirkpatrick, A universal equivalent circuit for carbon-based supercapacitors, Journal of Solid State Electrochemistry, 18 (2014) 1377-1387.

[44] R.P. Janek, W.R. Fawcett, A. Ulman, Impedance Spectroscopy of Self-Assembled Monolayers on Au(111): Evidence for Complex Double-Layer Structure in Aqueous NaClO4 at the Potential of Zero Charge, The Journal of Physical Chemistry B, 101 (1997) 8550-8558.

[45] P. Zoltowski, The error function for fitting of models to immittance data, Journal of Electroanalytical Chemistry and Interfacial Electrochemistry, 178 (1984) 11-19.

[46] B. Piela, P.K. Wrona, Capacitance of the gold electrode in 0.5 M H2SO4 solution: a.c. impedance studies, Journal of Electroanalytical Chemistry, 388 (1995) 69-79.

[47] J. Chang, J. Park, Y.K. Pak, J.J. Pak, Fitting Improvement Using a New Electrical Circuit Model for the Electrode-Electrolyte Interface, 2007 3rd International IEEE/EMBS Conference on Neural Engineering, 2007, pp. 572-574.

[48] R. De Levie, On porous electrodes in electrolyte solutions—IV, Electrochimica acta, 9 (1964) 1231-1245.

Figure 1

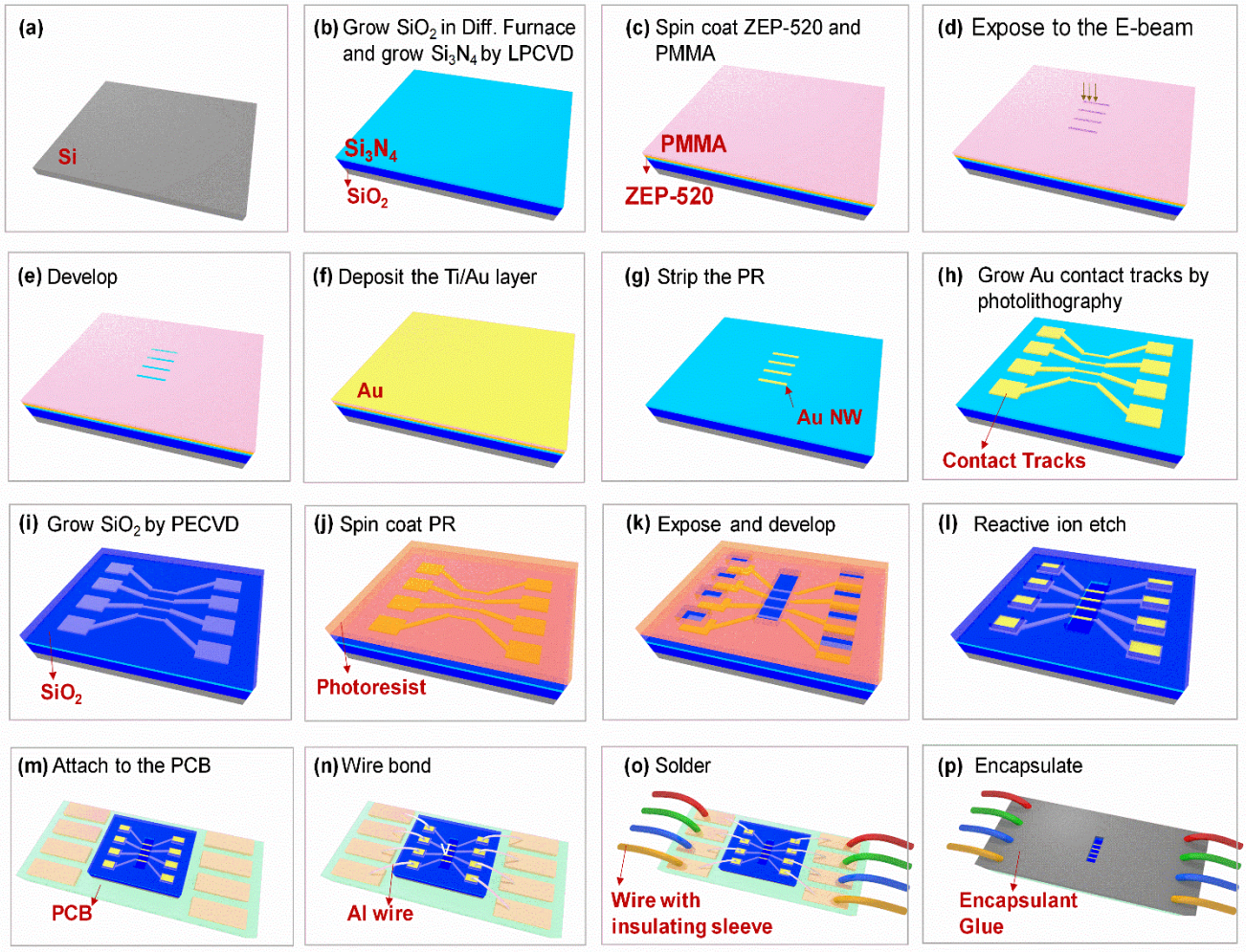

Figure 1. (a-p) A schematic diagram of the fabrication process of the on-chip suspended Au NW electrodes.

Figure 2

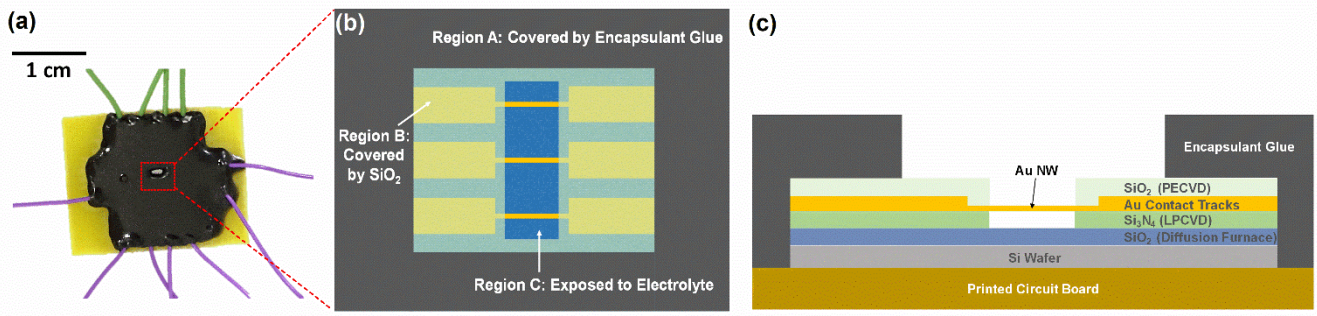

Figure 2. (a) The image of a final packaged device with the suspended Au NW as the working electrode. (b) The illustration of the top view illustration of the central part of the fabricated test device. (c) The illustration of the structure of test device (ignored the wire bonding and soldered contact wire).

Figure 3

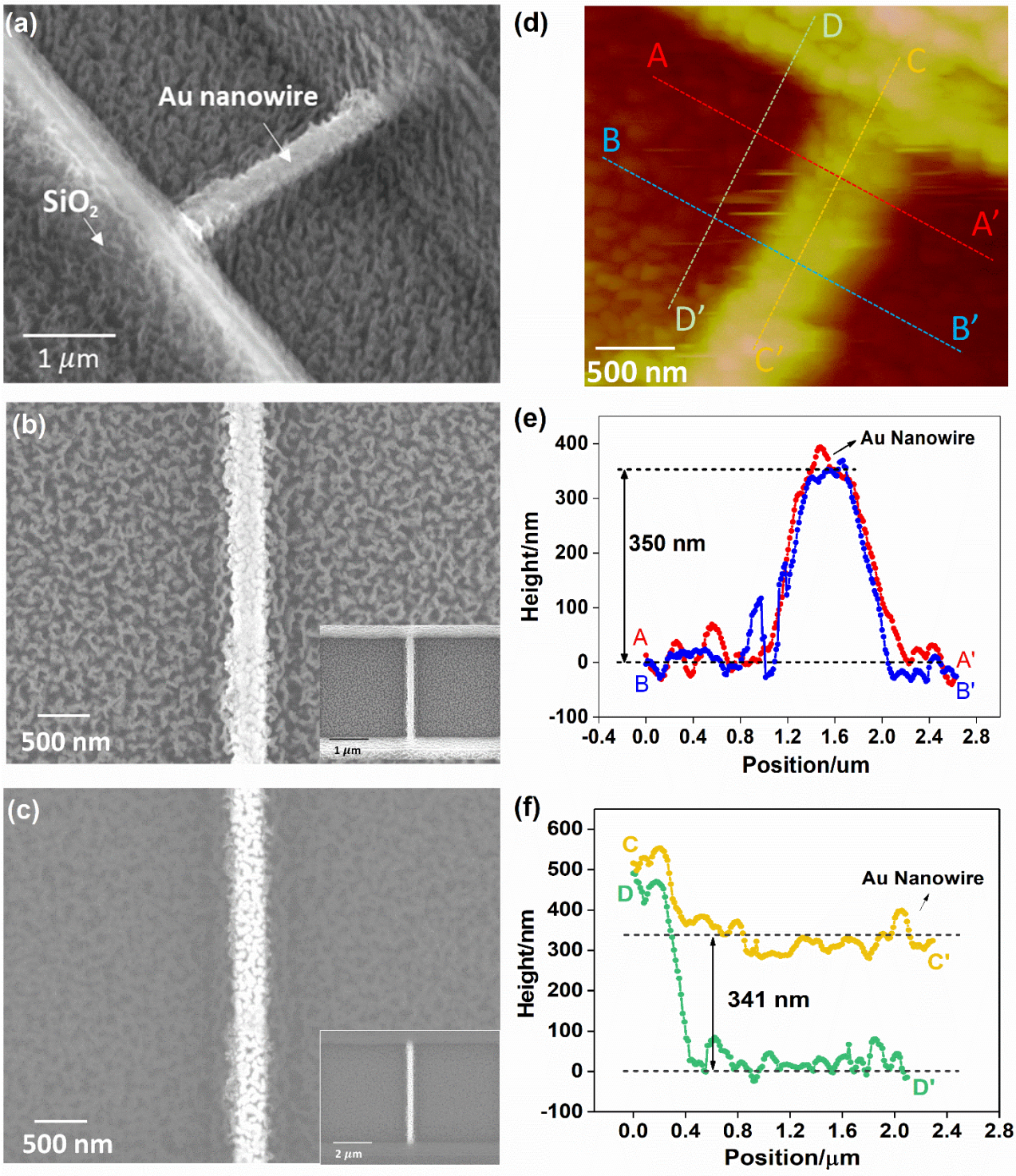

Figure 3. (a) The SEM image (lower electron detector) taken with a tilted angle of the Au NW electrode to illustrate its suspension status. The SEM images of the Au NW electrode with the

lower electron detector (b) and the backscattered electron detector (c) to illustrate its rough surface. (d) AFM image of a suspended nanowire with scanning lines AA' and BB' perpendicular to the NW's length direction, CC' along the nanowire surface and DD' crossing the substrate. (e) The scanned height profiles of lines AA' and BB'. (f) The scanned height profiles of lines CC' and DD'.

Figure 4

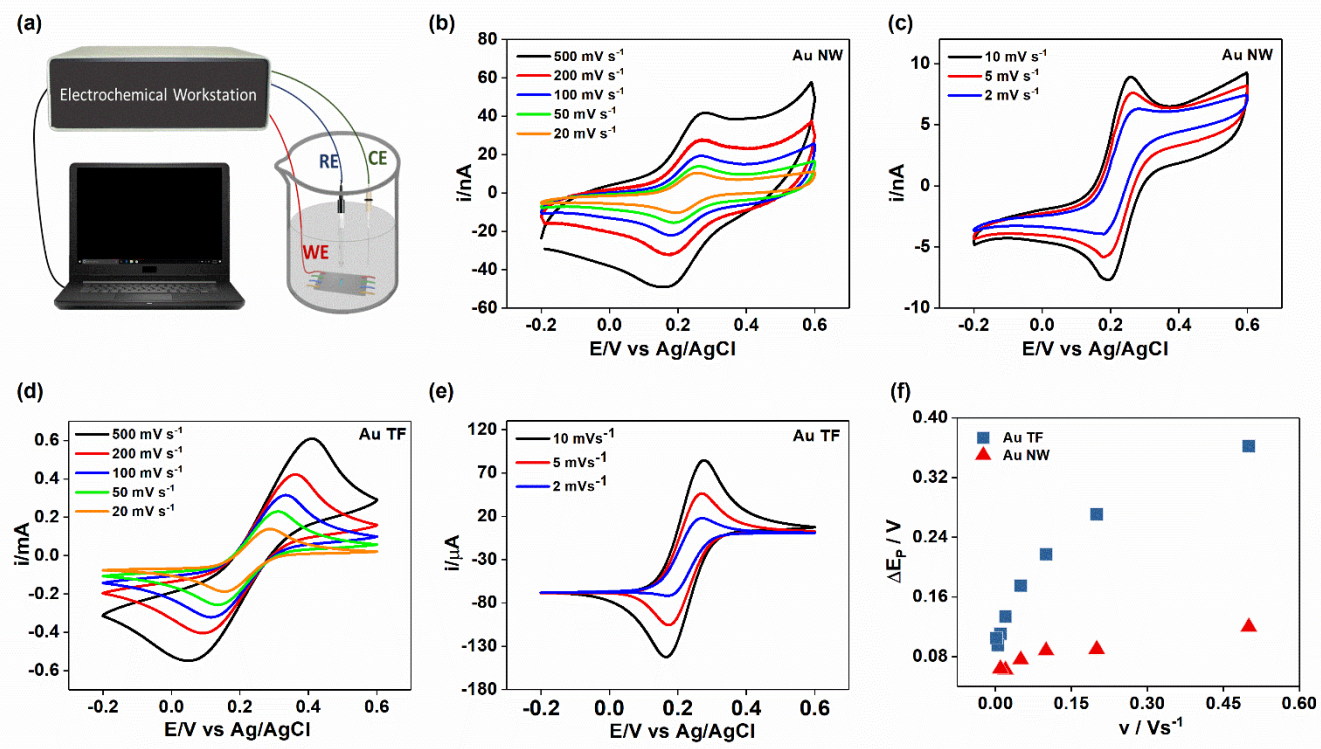

Figure 4. (a) The illustration of the experiment setup using the three electrode system. (b) The voltammograms of Au NW electrode in 20 mM $K_3[Fe(CN)_6]$ + 0.1 M KCl solution at scan rates that range from 500 mVs^{-1} to 20 mVs^{-1}. (c) The voltammograms of Au NW electrode in in 20 mM $K_3[Fe(CN)_6]$ + 0.1 M KCl obtained at 10 mVs^{-1}, 5 mVs^{-1} and 2 mVs^{-1}. (d) The voltammograms of Au TF electrode in 20 mM $K_3[Fe(CN)_6]$ + 0.1 M KCl solution at scan rates that range from 500 mVs^{-1} to 20 mVs^{-1}. (e) The voltammograms of Au TF electrode in in 20 mM $K_3[Fe(CN)_6]$ + 0.1

M KCl obtained at 10 mVs^{-1}, 5 mVs^{-1} and 2 mVs^{-1}. (f) Plots of the peak-to-peak potential separation, ΔE_p of the current peaks in Fig. 4(b, c, d, e) against scan rate.

Figure 5

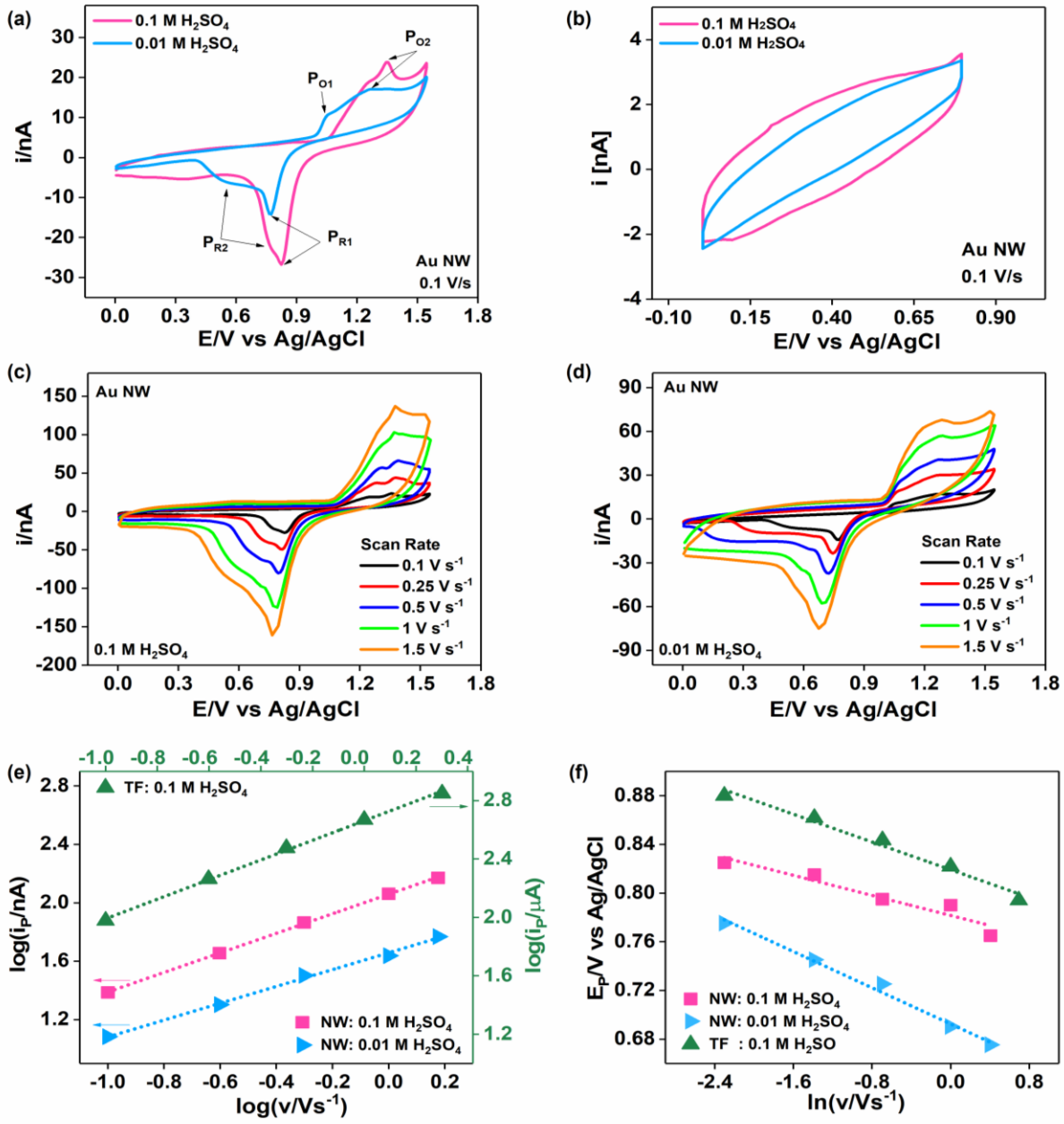

Figure 5. (a) The voltammograms of an Au NW electrode at a scan rate of 0.1 V s^{-1} in 0.1 M and 0.01 M H_2SO_4 solutions, respectively. (b) The voltammograms within the EDL region of an Au

NW electrode at a scan rate of 0.1 V s^{-1} in 0.1 M and 0.01 M H_2SO_4 solutions, respectively. (c) The voltammograms of Au NW electrode in 0.1 M H_2SO_4 solution at different scan rates. (d) The voltammograms of Au NW electrode in 0.01 M H_2SO_4 solution at different scan rates. (e) Plots of the logarithm of peak currents of peak P_{R1} (P_R for Au TF) against the logarithm of scan rate. (f) Plots of the peak potentials of P_{R1} (P_R for Au TF) against the natural logarithm of scan rate.

Figure 6

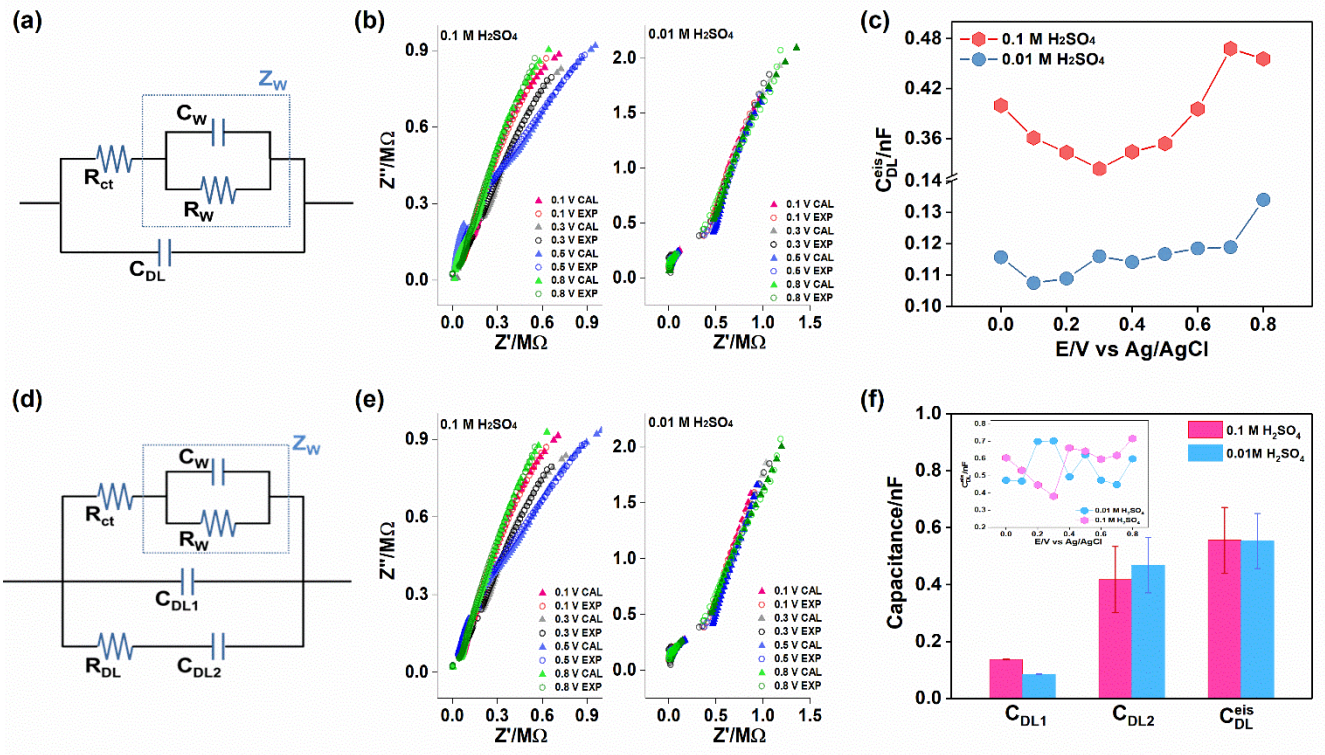

Figure 6. (a) The Illustration of the Kovacs model. (b) Measured impedance spectrum and fitted spectra (the Kovacs model) of the EIS results obtained in 0.1 M and 0.01 M H_2SO_4 solutions at different potentials, respectively. (c) Plots of the obtained values for C_{DL}^{eis} (the Kovacs model) against tested potentials. (d) The illustration of the modified Kovacs model. (e) Measured impedance spectrum and fitted spectra (the modified Kovacs model) of the EIS results obtained in 0.1 M and 0.01 M H_2SO_4 solutions at different potentials, respectively. (f) Plots of the average

values of C_{DL1}, C_{DL2} and C_{DL}^{eis} (the modified Kovacs model) in 0.1 M and 0.01 M H_2SO_4 solutions, respectively. The inset plots values of C_{DL}^{eis} (the modified Kovacs model) against tested potentials.

Figure 7

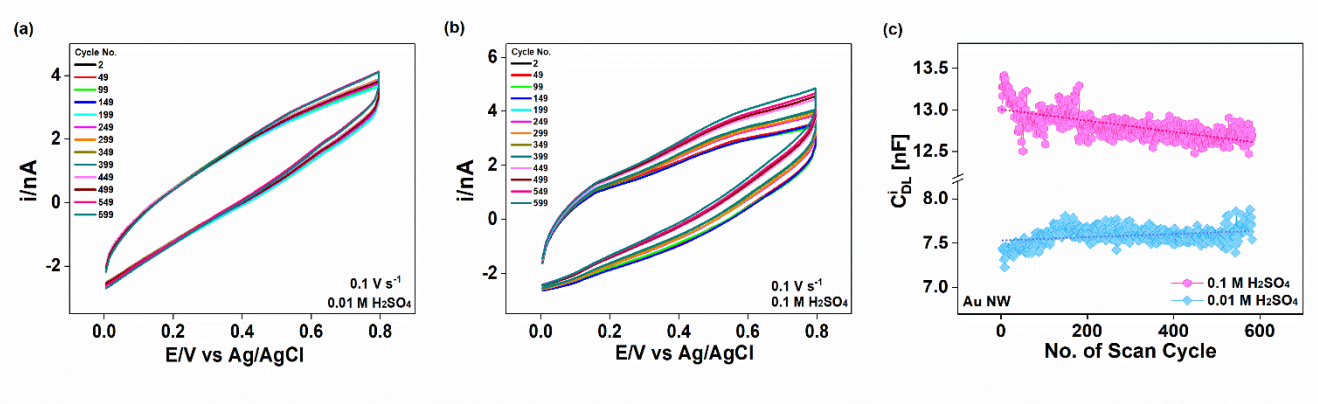

Figure 7. (a) The voltammograms of Au NW electrode in 0.01 M H_2SO_4 solution at different scan cycles. (b) The voltammograms of Au NW electrode in 0.1 M H_2SO_4 solution at different scan cycles. (c) Plots of the integrated capacitances against the number of scan cycle in 0.1 M and 0.01 M H_2SO_4 solutions, respectively.